arXiv:astro-ph/0208379v1 20 Aug 2002

Astrophysical Journal, in press

A 15-Kiloparsec X-Ray Disk in the Elliptical Galaxy NGC 1700

Thomas S. Statler and Brian R. McNamara

Department of Physics and Astronomy, 251B Clippinger Research Laboratories, Ohio University, Athens, OH 45701, USA

statler@ohio.edu, mcnamarab@ohio.edu

ABSTRACT

We present *Chandra* observations of the young elliptical galaxy NGC 1700. The X-ray isophotes are highly flattened between semimajor axes of 30″ and 80″, reaching a maximum ellipticity $\epsilon_X \approx 0.65$ at 60″ (15 kpc). The surface brightness profile in the spectrally soft, flattened region is shallower than that of the starlight, indicating that the emission comes from hot gas rather than stellar sources. The flattening is so extreme that the gas cannot be in hydrostatic equilibrium in any plausible potential. A likely alternative is that the gas has significant rotational support. A simple model, representing isothermal gas distributed about a particular angular momentum, can reproduce the X-ray morphology while staying consistent with stellar kinematics. The specific angular momentum of the gas matches that of the stars in the most isophotally distorted outer part of the galaxy, and its cooling time matches the time since the last major merger. We infer that the gas was acquired in that merger, which involved a pre-existing elliptical galaxy with a hot ISM. The hot gas carried the angular momentum of the encounter, and has since gradually settled into a rotationally flattened, cooling disk.

Subject headings: galaxies: cooling flows—galaxies: elliptical and lenticular, cD—galaxies: ISM—X-rays: galaxies—X-rays: ISM

1. Introduction

Much of what we know about the mass distributions in the outer parts of giant elliptical galaxies comes from X-ray observations of their hot interstellar media (ISM). Since the initial studies of M87 (Mathews 1978; Fabricant et al. 1980), mass profiles of several dozen systems have been derived from X-ray data (Loewenstein & White 1999, and references therein, for example), strengthening the case for the ubiquity of dark halos. All these results rely on the assumption that the gas is in hydrostatic equilibrium, an assumption that is difficult to validate. If hydrostatic equilibrium holds, the X-ray surface brightness must trace the projected potential. Conversely, if there is no plausible potential consistent with the morphology, then the gas cannot be in equilibrium. But the distinction between an implausible potential and one that is merely strange is not clear-cut. The quintessential example is NGC 720, whose X-ray isophotes, while rounder than the optical isophotes, are flatter than the projected stellar potential. Buote & Canizares (1994) were able to account for this difference by postulating a dark halo that was alarmingly flat, though not altogether implausible. Later studies making use of *ASCA* (Buote & Canizares 1998) and *Chandra* (Buote et al. 2002) data have shown that removing the contribution from stellar sources makes the remaining diffuse emission rounder, relaxing the constraints somewhat, but still implying a substantial halo flattening.

In the *Chandra* era of high resolution, luminous ellipticals continue to appear round in X-rays, even at small radii. This comes as some surprise in light of arguments by Mathews and collaborators that at least some of the gas should be rapidly rotating, and thus not in true hydrostatic equilibrium. Kley & Mathews (1995) pointed out that, since stellar evolution is a primary source of gas, the gas should retain the specific angular momentum of the stars, which is typically only a factor of a few below that required for rotational support. Cooling gas would therefore need to sink by only a modest factor in radius before becoming rotationally supported and forming a disk. These ideas were subsequently fleshed out in detailed simulations by Brighenti & Mathews (1996, 1997, collectively BM). However, a careful examination of archival *ROSAT* data by Hanlan & Bregman (2000) showed no indication of central X-ray disks, and in fact no significant difference between the distribution of X-ray and optical ellipticities, leading Brighenti & Mathews (2000) to propose a combination of heat conduction and mass dropout to explain the absence of the predicted structures.

In this paper we report on *Chandra* observations of the young elliptical NGC 1700. We find that this galaxy's X-ray isophotes are not merely flatter than the stellar potential, but flatter than the starlight—so flat, in fact, that the gas cannot be in hydrostatic equilibrium in any plausible potential. We describe the observations and reductions in § 2 below and the basic results in § 3. We then argue in § 4 that the gas is settling into a rotationally flattened cooling disk, similar to those predicted by BM, but much larger in scale. The high angular momentum and the long cooling time suggest that the gas was accreted in the last major merger. These points are reiterated, and their implications briefly discussed, in § 5.

2. Observations and Data Reduction

NGC 1700 is a relatively isolated elliptical in a loose group with the nearest companion, the spiral NGC 1699, at a projected distance of 100 kpc. An age of 3 ± 1 Gyr (Brown et al. 2000, hereafter B00) is inferred from photometric fine structure (Schweizer & Setizer 1992), stellar dynamics (Statler et al. 1996, hereafter SSC), globular cluster colors (Whitmore et al. 1997, B00), and absorption line indices (B00). The galaxy is photometrically ordinary inside 2 effective radii ($r_e = 14'' = 3.5$ kpc at 51.4 Mpc) but becomes very boxy farther out, the parallelogram-shaped outer isophotes accompanied by faint shells. Detailed stellar kinematics (SSC) show that the galaxy rotates nearly about its apparent minor axis, with a mean velocity that rises outward into the boxy region. Dynamical models imply a weakly triaxial oblate potential that is dark-matter dominated outside r_e (Statler et al. 1999, hereafter SDS).

NGC 1700 was observed on 2000 November 3–4 with the ACIS instrument on *Chandra.* The galaxy was imaged on the S3 detector, offset from the nominal aimpoint by 1 arcminute in order to center it on Node 1. The spacecraft roll angle of 59° placed NGC 1699 on S2; however, no emission was detected from NGC 1699, and no other bright or extended sources were seen by any of the active detectors. We confine this discussion to the data from S3, for which the total corrected exposure time was 42,798 s.

The data were reduced and calibrated using CIAO 2.1.3 and CALDB 2.7, as follows: The level 1 event file was first reprocessed with the CALDB 2.7 gain map and PHA randomization turned on. The level 2 event file was rebuilt and the 'acis_detect_afterglow' correction removed, then filtered to retain S3 events between 0.3 and 10.0 keV. The resulting lightcurve showed no strong background flares, but substantial weak flaring and a gradual increase in the background level. We chose not to use 'lc_clean' and 'make_acisbg' to determine the background because these procedures would have discarded 60–70% of the data. Since the galaxy is small, we opted to keep the full exposure and derive backgrounds from source-free regions on the

same node of S3. Thus only the GTI filters from the pipeline "flt1" file were applied to the data and used to calculate the aspect histogram.

Flux calibrated images were derived by computing instrument and exposure maps at single energies spaced by 100 eV, then extracting 10 eV-wide energy slices from the event file, calibrating each slice with the nearest maps, and summing the results. We produced flux and counts images in three energy bands, soft (0.3–0.8 keV), hard (0.8–2.7 keV), and full (0.3–2.7 keV). Visual inspection of images with different energy cuts showed no noticeable emission from the galaxy above 2.7 keV. The division at 0.8 keV was chosen to put approximately equal numbers of counts in the soft and hard bands. We also produced a 0.5–2.0 keV image to compare with *ROSAT* and *ASCA* data on other systems. Adaptively smoothed images from the inner 512×512 pixel region were derived using the 'csmooth' task. The smoothing map was determined by running the task on the counts image, with the minimum and maximum S/N per smoothing element set to 4 and 5 respectively. The task was then rerun on the flux image using this map.

Profiles of surface brightness and isophotal ellipticity were extracted from the counts images by three different methods. In the first, the full-resolution images were further binned at scales of 2×2, 4×4, 8×8, and 16×16 pixels, and elliptical isophotes were fitted using the 'ellipse' task in STSDAS. The center was held fixed at the centroid of the 4 brightest pixels in the full band image, and the ellipticity was a free parameter. The major axis position angle (PA) was taken to be either freely variable or fixed at 90°, the two choices giving similar results; we show below the results for fixed PA. At each binning scale, converged fits were found over a range of semimajor axis (a). The results agreed to within the statistical errors where the ranges overlapped. The final ellipticity and PA profiles were pieced together so as to sample the profiles as densely as possible while ensuring that the data points remain statistically independent. In the second approach, the 'ellipse' task was run on the adaptively smoothed images. We consider this a dangerous alternative because the smoothing scale can vary along a fitted isophote, and consecutive points in the profiles are not independent. In the third approach, we applied an iterative algorithm that diagonalizes the spatial second-moment tensor of the photon counts in a thin elliptical ring and manipulates the axis ratio until the eigenvalues match those for a constant density ring of the same shape. This algorithm was applied to the unbinned, unsmoothed, full-resolution image. Its disadvantage is that errors in the fitted parameters can be determined only by Monte Carlo simulation. All three approaches gave results that are consistent within the Poisson noise, and so we have chosen to present the results from the first approach, where the statistical errors are best understood.

Spectra were extracted from various regions in the galaxy and from two square background regions near the ends of Node 1 on S3. Because the galaxy is faint—about 3400 counts in the full band image—spectra from different subregions are not distinguishable, and so we discuss only the total spectrum extracted in a 90″ circle, excluding three point sources. Single response matrix and auxiliary response files were computed at the center of the galaxy image and used for both galaxy and background spectra.

3. Results

3.1. Flux and Luminosity

The total flux in the full band is $F_{0.3-2.7} = (2.64 \pm 0.10) \times 10^{-13}\,\mathrm{erg\,cm^{-2}\,s^{-1}}$ (1σ errors). At a distance of 51.4 Mpc [$H_0 = 75\,\mathrm{km\,s^{-1}\,Mpc^{-1}}$; Whitmore et al. (1997)], this corresponds to a luminosity $L_{0.3-2.7} = (8.37 \pm 0.32) \times 10^{40}\,\mathrm{erg\,s^{-1}}$. These results include a correction for Galactic absorption computed from the best-fit spectral model described in § 3.3 below.

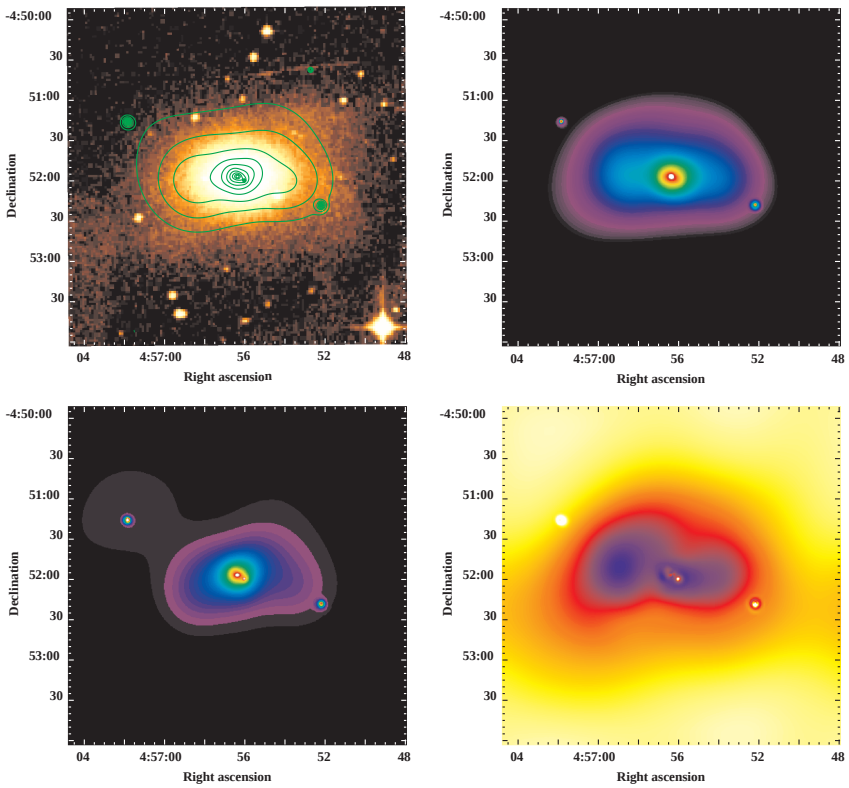

Fig. 1.— Adaptively smoothed, flux-calibrated X-ray images of NGC 1700: (*a; top left*) Contours of the full band (0.3–2.7 keV) image overlaid on the optical Digital Sky Survey image. In the DSS image, the apparent structure along the left edge and the streak northwest of center are plate defects, but the boxiness of the galaxy is real. (*b; top right*) Soft band image (0.3–0.8 keV) showing strongly disk-like emission 20″–50″ from the center. (*c; bottom left*) Hard band image (0.8–2.7 keV). (*d; bottom right*) Hard/soft flux ratio image; the ratio spans a range from 0.93 (blue) to roughly 3.2 in background-dominated regions (yellow). The central "squiggle" is a smoothing artifact.

To compare with existing data, we use a bandpass of 0.5–2.0 keV, to agree with Brown & Bregman (1998). Since there is virtually no flux above 2.0 keV, this choice also matches the 0.5–10.0 keV *ASCA* bandpass (Matsushita et al. 2000). We find $F_{0.5-2.0} = (1.94 \pm 0.06) \times 10^{-13}\,\mathrm{erg\,cm^{-2}\,s^{-1}}$, implying $L_{0.5-2.0} = (6.12 \pm 0.19) \times 10^{40}\,\mathrm{erg\,s^{-1}}$. At this distance, the blue luminosity is $L_B = 6.5 \times 10^{10} L_\odot$. This puts NGC 1700 (with a correction for different assumed H_0) less than 1σ below the mean L_X-L_B relation of Brown & Bregman (1998).

3.2. Morphology

Figure 1a shows contours of the adaptively smoothed, full-band image, plotted on the optical image from the Digital Sky Survey. The optical image shows the transition from the elliptical, slightly disky, inner region to the parallelogram-shaped outer region, beginning roughly 30″ from the center. Deeper imaging (Brown et al. 2000) shows the boxiness reaching a maximum and apparent tidal fine structure appearing at radii near 100″. The overlaid contours show the striking X-ray morphology of this system: between an elliptical inner zone and a somewhat boxy outer zone, the X-ray isophotes are highly flattened—far flatter

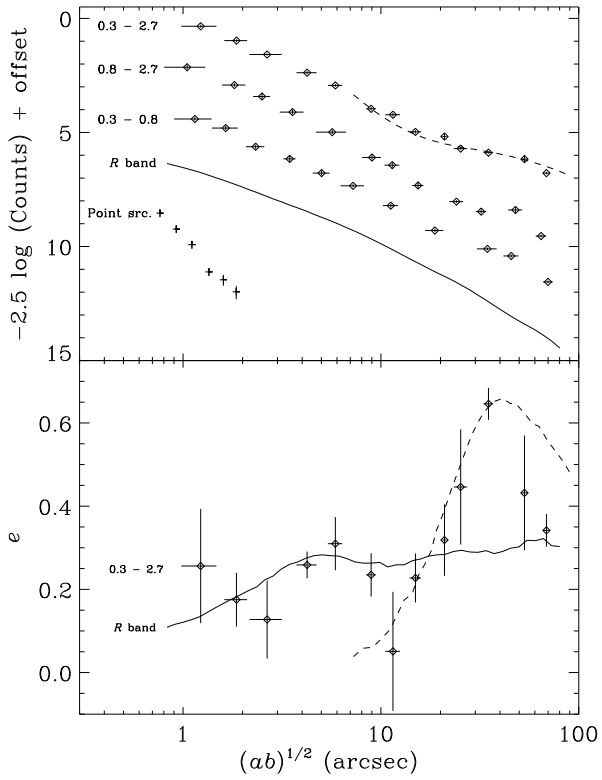

Fig. 2.— Surface brightness (*top*) and isophotal ellipticity (*bottom*) profiles of NGC 1700, plotted in terms of isophotal mean radius $a(1-\epsilon)^{1/2}$. Points with error bars show X-ray data in the soft, hard, and full bands as indicated. Horizontal error bars indicate the spatial bin size (see § 2). Solid curves show optical R-band profiles for comparison. The profile of a point source is also shown in the upper plot. Dashed curves indicate fitted profiles using the model described in § 4.2.

than the starlight—over a factor of 2 in radius. The flattening is most prominent in the soft emission, as can be seen by comparing the smoothed soft-band and hard-band images in Figure 1b and 1c. The ratio of the hard to the soft image is shown in Figure 1d. The ratio image reinforces the basic result that the softest emission is the flattest emission; the most flattened regions coincide with the lowest hardness ratios.

The photometric profiles are shown in figure 2. The surface brightnesses in the soft, hard, and full bands are plotted in the upper panel, along with the R band profile (Franx et al. 1989) for comparison. The bottom panel shows the isophotal ellipticities in the X-ray (full band) and optical. The profiles show a natural division at a mean radius $a(1-\epsilon)^{1/2} \approx 20''$ separating an inner region, in which the X-ray surface brightness falls off slightly more steeply than the starlight and the X-ray and optical ellipticities are nearly equal, from an intermediate-radius region where the X-ray surface brightness levels out and the ellipticity increases to $\epsilon_X \approx 0.65$. One can also delineate an outer region at mean radii beyond $50''$, where the surface brightness again falls and the ellipticity returns approximately to that of the starlight. In the inner region, the soft, hard, and full profiles can be fitted by β models with $\beta = 0.45$, 0.49, and 0.47, respectively. The difference is statistically significant; the hardness ratio increases *inward*, with $d\ln(SB_{0.8-2.7}/SB_{0.3-0.8})/d\ln a = -0.23 \pm 0.03$. At the center, there is no indication of an unresolved nuclear source, as can be seen by comparing the galaxy profiles with the point source profile in the top of figure 2.

The four point sources in Figure 1a may or may not be associated with NGC 1700. The source nearest the center falls within 0.″2 of one of the globular cluster candidates (#22) identified by Whitmore et al. (1997), if we assume that the X-ray and optical centers coincide. However, this source is invisible in the soft band, indicating that it is probably highly absorbed. Since the upper limit on NGC 1700's H I mass is $3.5 \times 10^9 M_\odot$ (Huchtmeier 1994), we surmise that this source is more likely a background AGN. The remaining sources, at the distance of NGC 1700, would have luminosities between 5×10^{38} and $5 \times 10^{39}\,\mathrm{erg\,s^{-1}}$, comparable with the brightest sources resolved in NGC 4697 (Sarazin, Irwin, & Bregman 2001). On the other hand, the density of sources is similar to that in the rest of the field, so there is no compelling reason to conclude that they cannot be background objects.

3.3. Spectrum

We use a variety of models in XSPEC to fit the total spectrum. Satisfactory fits ($0.98 < \chi^2/\mathrm{d.o.f.} < 1.1$) are obtained with absorbed MEKAL models, while both power-law and cooling flow models fail. In the absorbed MEKAL fits, the Galactic H I column is fixed at $N_\mathrm{H} = 4.8 \times 10^{20}\,\mathrm{cm^{-2}}$ (Dickey & Lockman 1990). Because the ACIS-S calibration is still somewhat uncertain at low energies (M. Wise and C. Sarazin, private communications), we apply cutoffs to the spectrum at either 0.3 or 0.5 keV. The free parameters are the gas temperature T and metallicity Z; in some fits the redshift is also allowed to vary to correct for residual energy calibration errors. We find that the systematic uncertainties are on the order of the statistical errors. The grid of models results in temperatures in the range 0.44–0.49 keV and metallicities in the range 0.47–$0.55 Z_\odot$, with statistical errors of 0.02 and 0.2 respectively. We conservatively estimate $T = (0.47 \pm 0.03)$ keV and $Z = (0.5 \pm 0.3) Z_\odot$.

4. Discussion

4.1. Can the Gas be in Hydrostatic Equilibrium?

The X-ray emission from elliptical galaxies comes from a mixture of stellar sources and diffuse gas, in varying proportions. Inside r_e, NGC 1700's X-ray isophotes have the same ellipticity as the starlight, hinting that stellar sources may dominate. But we do not see the hard spectral component characteristic of low-mass X-ray binaries. We therefore cannot determine whether stellar sources are important in the inner regions. Farther out, the situation is different. The X-ray isophotes reach ellipticities $\epsilon_X \approx 0.65$ at a major axis distance of approximately 60″ (15 kpc). At these radii, the optical isophotes have $\epsilon_\mathrm{opt} \approx 0.3$, and the X-ray surface brightness falls off much less steeply than the starlight. There is little doubt that this emission is coming from a diffuse ISM.

All studies using X-ray emission to constrain galaxy mass profiles rely on the assumption that the diffuse ISM is in hydrostatic equilibrium. Regardless of the equation of state, this condition requires that the surfaces of constant density, pressure, temperature, and consequently X-ray emissivity all coincide with the equipotentials, and therefore that the X-ray surface brightness traces the shape of the projected potential.[1]

[1]Because there is only one plane normal to a given line through a given point, the level surfaces of two functions must coincide if and only if their gradients are everywhere parallel (or antiparallel) to each other. The hydrostatic equation, $\nabla P + \rho \nabla \Phi = 0$, implies that the level surfaces of P and Φ coincide. Taking the curl gives $\nabla\rho \times \nabla\Phi = 0$; thus the ρ and Φ level surfaces also coincide. P must therefore be expressible as $P(\rho)$, and any equation of state $P = P(\rho, T)$ then implies that $T = T(\rho)$. (We

We can test the assumption of hydrostatic equilibrium in NGC 1700 using axisymmetric models, since the galaxy's stellar velocity field implies a nearly oblate potential (SDS). First, we estimate the stellar potential using the approach of Binney et al. (1990, see § 3.1.1 of SDS for details). The stellar potential has $\epsilon \approx 0.1$ for lines of sight near the equatorial plane, and we calculate only the edge-on case, since at lower inclinations the gas would need to be even flatter than it appears. We then ask whether any plausible dark matter distribution can be added so as to give the total potential a flattening $\epsilon_\Phi > 0.6$ at mean radii of $35''$. Intuition argues that this will require a dark mass at least as large as the stellar mass, highly flattened and not too centrally concentrated lest its monopole term be too large.

The largest flattening for a given dark mass would be produced by a dark halo that is a disk. A good example is the Kuzmin (1956) disk, whose surface density is given by

$$\Sigma(R) = \Sigma_0[1 + (R^2/r_0^2)]^{-3/2}. \tag{1}$$

The constant Σ_0 is the central density and r_0 is the radius within which $\Sigma \sim$ constant. Since the Kuzmin disk has both a very low central concentration and a steep outer cutoff, one would expect it to be best able to produce a substantial flattening over a limited range of radii. We find that the minimum mass able to generate the correct flattening is $2 \times 10^{12}(M/L_B)_\star M_\odot$, where stellar mass-to-light ratios $(M/L_B)_\star \approx 4$ are needed to fit the kinematics at small radii (Bender et al. 1992). However, this case requires $r_0 \approx 90''$, which implies a circular velocity curve rising to $\sim 250(M/L_B)_\star \,\mathrm{km\,s^{-1}}$ at $R = 50''$. This is inconsistent with the observed kinematics (SSC). No Kuzmin disk of any mass can yield $\epsilon_\Phi \geq 0.6$ if $r_0 < 50''$, and all Kuzmin disks with $r_0 > 50''$ massive enough to flatten the potential produce rotation curves inconsistent with the stellar kinematics.

To try to preserve the rotation curve, we replace the Kuzmin disk with Schwarzschild (1993) logarithmic potentials of various flattenings. These potentials have a constant circular velocity at all radii, and are generated by strictly positive mass densities down to quite large flattenings. We find, however, that no Schwarzschild density of any flattening has a potential with $\epsilon_\Phi > 0.35$, simply because they are too centrally concentrated. Other popular halo models, such as the NFW (Navarro et al. 1995) and Hernquist (1990) models, are more centrally concentrated than the Schwarzschild model and fail in the same way. Finally, a linear combination of Schwarzschild and Kuzmin models suffers from the same problem as the pure Kuzmin disks, since the disk potential must be dominant to provide the bulk of the flattening.

We conclude that there is no plausible potential in which the gas can be in hydrostatic equilibrium and be as flattened as the X-ray isophotes indicate. Either the gas is well out of equilibrium, or the equilibrium is hydrodynamical rather than hydrostatic, with angular momentum—i.e., bulk rotation of the gas—playing an important role.

4.2. An Accreted Disk

At large radii, NGC 1700 shows clear optical signatures of a past merger, including shells and prominent boxiness (Franx et al. 1989; Whitmore et al. 1997; Brown et al. 2000). In deep exposures the galaxy becomes parallelogram-shaped. Franx et al. (1989) conjectured that the long diagonal of the parallelogram marks an inclined outer disk or ring, while Brown et al. (2000) interpreted the brightness enhancement along this direction as a pair of symmetric tidal tails. SSC argued that the entire parallelogram could be produced by

---

thank the referee for this demonstration.)

a broad, differentially precessing ring seen in projection. By requiring that this structure be prominent at large radii but phase-mixed beyond visibility at smaller radii, SSC estimated a dynamical age of 2–$4h^{-1}$ Gyr, consistent with other techniques (Brown et al. 2000).

Since both absorption line indices and globular cluster colors also indicate few-Gyr ages, NGC 1700's most recent merger probably involved a substantial amount of cold gas and star formation. Brown et al. (2000) suggest that the merger involved two spirals, but there is no reason to exclude a merger of a spiral and a pre-existing elliptical with a hot ISM. Such a merger would dump a load of already-hot gas into the common potential well, at an angular momentum characteristic of the galaxy-galaxy encounter. At sufficiently low densities, this gas would not be channeled to the center as the cold gas would, but would instead settle into a rotationally flattened cooling disk. We propose that the flattened X-ray structure in NGC 1700 is exactly such a disk, acquired in the same merger that created the optical boxiness and tidal features.

We can demonstrate the plausibility of this scenario with a simple model. First, imagine a population of collisionless particles dumped into the galactic potential at a fixed kinetic temperature, distributed about a finite angular momentum L_0. After phase mixing, this population would take on a phase space distribution function (DF) given by

$$f \propto e^{-\beta E} e^{-\alpha (L_z - L_0)^2}, \tag{2}$$

where E and L_z are the energy and z component of angular momentum (both per unit mass), and α and β are constants. The first factor gives an isothermal distribution in energy, while the second applies a Gaussian bias around L_0. We adopt an axisymmetric model potential,

$$\Phi(R,z) = \frac{V_c^2}{2} \ln\left[1 + \frac{R^2 + (z/q)^2}{R_c^2}\right], \tag{3}$$

where (R, ϕ, z) are cylindrical coordinates, V_c is the asymptotic circular velocity, and R_c and q are the core radius and flattening. This potential gives a flat circular velocity curve for $R \gg R_c$. The actual rotation velocity of the material follows from the DF:

$$\langle v_\phi \rangle = \frac{L_0 R}{R^2 + R_0^2}, \tag{4}$$

where $R_0 \equiv (\beta/2\alpha)^{1/2}$. We could calculate the density by integrating over velocities, but there is no need because the collisionless model is unrealistic. Its velocity distribution becomes strongly anisotropic for $R \gtrsim R_0$, while in reality collisions should isotropize the pressure in, at most, a dynamical time.

In the simplest rotating equilibrium, the gas pressure P and density ρ should obey the hydrostatic equations with an extra term for the bulk velocity:

$$\frac{\partial P}{\partial R} + \rho\left(\frac{\partial \Phi}{\partial R} - \frac{\langle v_\phi \rangle^2}{R}\right) = 0, \qquad \frac{\partial P}{\partial z} + \rho \frac{\partial \Phi}{\partial z} = 0, \tag{5}$$

Here we are again assuming axisymmetry, and also neglecting shear viscosity. Notice that the hydrostatic equations do not tell us how to choose the mean velocity $\langle v_\phi \rangle$. But if we adopt the rotation curve from the collisionless model [equation (4)] with the potential of equation (3), and assume an isothermal equation of state, then equations (5) can be integrated analytically to obtain the density. Letting the volume emissivity ν then be proportional to ρ^2, we find

$$\nu = \nu_0 \exp\left(\frac{A}{1 + R_0^2/R^2}\right)\left(1 + \frac{R^2 + z^2/q^2}{R_c^2}\right)^{-B}. \tag{6}$$

In equation (6), ν_0 is the central emissivity, R_0 is the radius of the peak of the rotation curve, $A \equiv (\mu m_{\rm H}/kT)(L_0/R_0)^2$ measures the angular momentum bias, and $B \equiv (\mu m_{\rm H}/kT)V_c^2$ (with μ and $m_{\rm H}$ the mean molecular weight and hydrogen mass) describes the depth of the potential relative to the temperature.

We project the emissivity of equation (6) for a line of sight in the equatorial plane, and fit elliptical isophotes. The dashed curves in Figure 2 show the isophotal profiles in the relevant range of radii for a model with $A = 8.0$, $B = 2.3$, and $R_0 = 50''$. The potential is spherical ($q = 1$), with R_c set small enough that it does not influence the results. The model does a credible job of reproducing both profiles, over nearly a decade in mean radius, despite its extreme simplicity. As a check, we can use the value of B and the gas temperature to predict the circular velocity. Assuming $\mu = 0.6$, we obtain $V_c = 420\,{\rm km\,s^{-1}}$. Treating the dark halo as a singular isothermal sphere, this implies a velocity dispersion $\sigma_{\rm halo} = 2^{-1/2}V_c = 290\,{\rm km\,s^{-1}}$. The stellar component, having formed dissipationally, is dynamically colder than the halo and should have a lower dispersion. If we model both stars and halo as constant-dispersion systems with power-law density profiles having logarithmic slopes of -3.5 and -2 respectively, we predict $\sigma_{\rm stars}/\sigma_{\rm halo} = 2/7^{1/2}$ (Carlberg 1994). This implies $\sigma_{\rm stars} = 220\,{\rm km\,s^{-1}}$, which compares favorably with the measured peak dispersion (outside the cold counterrotating core) of $230\,{\rm km\,s^{-1}}$ (SSC).

At the radius of maximum flattening ($56''$), the gas in the model has a mean rotation velocity of $270\,{\rm km\,s^{-1}}$, about two-thirds of the circular velocity. This gives it a specific angular momentum twice as large as that of the stars at the same radius. The stellar rotation velocity $V_* \approx 150\,{\rm km\,s^{-1}}$ at the outermost measured point ($65''$). If we assume that V_* remains approximately constant to larger radii, then the stars carrying the same specific z angular momentum as the gas would be found at $R \approx 90''$, coinciding with the maximum distortions of the optical isophotes. We would naturally expect such a concordance if the stars making up the stellar ring and the X-ray gas were accreted together.

Finally, in order to settle into a disk, the gas must have had time to cool. At $T \approx 0.5\,{\rm keV}$ and $Z \approx Z_\odot/2$, the cooling function $\Lambda \approx 6 \times 10^{-15}\,{\rm keV\,cm^3\,s^{-1}}$ (Böhringer & Hensler 1989). Normalizing to the observed surface brightness at $56''$, we find the electron density in the model at $R = 14\,{\rm kpc}$ to be $3 \times 10^{-3}\,{\rm cm^{-3}}$ in the midplane of the disk. The cooling time is therefore $t_{\rm cool} \approx 3\,{\rm Gyr}$, which is equal to the dynamical age of the merger debris. Thus, enough time has elapsed since the merger for the gas to have partially cooled and settled, but not so much that it would have sunk completely to the bottom of the potential well.

5. Conclusions

Chandra observations of NGC 1700 show extended X-ray emission that is dominated by a hot ISM. The gas is distributed in a flattened structure that is inconsistent with hydrostatic equilibrium in any plausible potential. A simple model in which gas at a single temperature, centered around a particular angular momentum, is dispersed in a logarithmic potential can account for the gross X-ray morphology and be consistent with stellar kinematics. The angular momentum of the gas matches that of the stars in the isophotally distorted outer part of the galaxy, and its cooling time matches the dynamical age of the last merger. We infer that the gas was acquired in that merger, carrying the angular momentum of the encounter, and is settling into a rotationally flattened, cooling disk.

The presence of a rotationally supported disk in this object, and the growing evidence for shocks and bubbles in the ISM of elliptical galaxies (Jones et al. 2002; Finoguenov & Jones 2001) casts doubt on the assumption that elliptical galaxies are simple, hydrostatic systems. Mass profiles derived from X-ray data and hydrostatic models may therefore be in error, even in those systems that appear symmetric. A modest

degree of rotational support in the gas may significantly affect the shape of the inferred mass distribution, depending on how the angular momentum is distributed. In the models of § 4.2, rotational support increases outward interior to R_0 and decreases outward beyond this radius. Applying a hydrostatic model would therefore lead to a mass profile that is too centrally concentrated. Interestingly, galaxy cluster mass profiles are found, in some cases (David et al. 2001; Nevalainen et al. 2001), to be unusually concentrated compared to the expected NFW (Navarro et al. 1995) profile. Whether this discrepancy could also stem from gas rotation remains to be seen.

The authors are grateful to Yousaf Butt, Pat Slane, and the staff of the CXC for their skillful operation of *Chandra*, and to Mike Wise, Craig Sarazin, Duncan Forbes, Joe Shields, and Steven Diehl for helpful suggestions and comments. Support for this work was provided by grant GO1-2094X from the CXC.

REFERENCES

Bender, R., Burstein, D., & Faber, S. M. 1992, ApJ, 399, 462

Binney, J., Davies, R. L., & Illingworth, G. D. 1990, ApJ, 361, 78

Böhringer, H. & Hensler, G. 1989, A&A, 215, 147

Brighenti, F. & Mathews, W. G. 1996, ApJ, 470, 747

Brighenti, F. & Mathews, W. G. 1997, ApJ, 490, 592

Brighenti, F. & Mathews, W. G. 2000, ApJ, 539, 675

Brown, B. A. & Bregman, J. N. 1998, ApJ, 495, L75

Brown, R. J. N., Forbes, D. A., Kissler-Patig, M., Brodie, J. P. 2000, MNRAS, 317, 406

Buote, D. A. & Canizares, C. R. 1994, ApJ, 427, 86

Buote, D. A. & Canizares, C. R. 1998, MNRAS, 298, 811

Buote, D. A., Jeltema, T. E., Canizares, C. R., & Garmire, G. P. 2002, ApJ, in press (astro-ph/0205469)

Carlberg, R. 1994, ApJ, 433, 468

David, L. P., Nulsen, P. E. J., McNamara, B. R., Forman, W., Jones, C., Ponman, T., Robertson, B., & Wise, M. 2001, ApJ, 557, 546

Dickey, J. M. & Lockman, F. J. 1990, ARA&A, 28, 215

Fabricant, D., Lecar, M., & Gorenstein, P. 1980, ApJ, 241, 552

Finoguenov, A., & Jones, C. 2001, ApJ, 547, L107

Franx, M., Illingworth, G. D., & Heckman, T. 1989, AJ, 98, 538

Hanlan, P. C. & Bregman, J. N. 2000, ApJ, 530, 213

Hernquist, L. 1990, ApJ, 356, 359

Huchtmeier, W. K. 1994, A&A, 286, 389

Jones, C., Forman, W., Vikhlinin, A., Markevitch, M., David, L., Warmflash, S., Murray, S., & Nulsen, P.E.J. 2002, ApJ, 567, L115

Kley, W. & Mathews, W. G. 1995, ApJ, 438, 100

Kuzmin, G. 1956, Astron. Zh., 33, 27

Loewenstein, M. & White, R. E., III 1999, ApJ, 518, 50

Mathews, W. G. 1978, ApJ, 219, 413

Matsushita, K., Ohashi, T., & Makishima, K. 2000, PASJ, 52, 685

Mestel, L. 1963, MNRAS, 126, 553

Navarro, J. F., Frenk, C. S., & White, S. D. M. 1995, MNRAS, 275, 720

Nevalainen, J., Kaastra, J., Parmar, A. N., Markevitch, M., Oosterbroek, T., Colafrancesco, S., & Mazzotta, P. 2001, A&A, 369, 459

Romanowsky, A. J. & Kochanek, C. S. 1998, ApJ, 493, 641

Sarazin, C. L., Irwin, J. A., & Bregman, J. N. 2001, ApJ, 556, 533

Schwarzschild, M. 1993, ApJ, 409, 563

Schweizer, F. & Seitzer, P. 1992, AJ, 104, 1039

Statler, T. S., Dejonghe, H., & Smecker-Hane, T. 1999, AJ, 117, 126 (SDS)

Statler, T. S., Smecker-Hane, T., & Cecil, G. 1996, AJ, 111, 1512 (SSC)

Whitmore, B. C., Miller, B. W., Schweizer, F., & Fall, S. M. 1997, AJ, 115, 1797

This preprint was prepared with the AAS LaTeX macros v5.0.